Journal of Computational Physics **155,** 26–53 (1999)
Article ID jcph.1999.6328, available online at http://www.idealibrary.com on IDEAL®

Free-Surface Flow Simulation Using *hp*/Spectral Elements

Iain Robertson and Spencer Sherwin

Department of Aeronautics, Imperial College of Science Technology and Medicine, Prince Consort Road, South Kensington, London SW7 2BY, United Kingdom
E-mail: i.robertson@ic.ac.uk, s.sherwin@ic.ac.uk

Received December 7, 1998; revised June 30, 1999

Computational instabilities inherent in the solution of inviscid, incompressible free-surface flow have been apparent for some time and different techniques have been used to overcome them. In this paper we attempt to explain why these instabilities occur and in doing so, a method is developed to study the spatially semi-discrete eigenvalues and eigenvectors which govern the stability of the system. It is found that the asymmetric spatial discretisation of the fluid domain causes the instabilities. After mechanisms for stability are recognised and implemented, unsteady, inviscid, incompressible, linear and non-linear free-surface flow is simulated using a *hp*/spectral element code, ensuring fast convergence, which incorporates arbitrary Lagrangian–Eulerian (ALE) techniques to decrease deformation of the computational mesh.

Key Words: hp/spectral finite elements; free-surface; stability analysis.

1. INTRODUCTION

The linear, free-surface motion of an inviscid, incompressible fluid has been solved exactly for simple finite depth water waves, e.g., travelling and standing waves [17] and analytical approximation techniques have enabled the solution of more complicated linear and low order non-linear systems [27, 20]. Numerical techniques have allowed the solution of non-linear free-surface motion commonly involving submerged complex geometries [35] and also surface piercing structures [1]. The finite element technique, in particular, has been found to be very efficient in the solution of free-surface problems [1, 34] and the new *hp*/spectral finite element technique is capable of very rapid convergence rates [9, 28], which coupled with the ability to handle complex geometries [26, 5] make it a worthwhile tool to aid the simulation of gravity waves.

A common theme with most of the finite element computations is the use of a smoothing technique to inhibit the formation of the free-surface saw-tooth pattern, which is

0021-9991/99 $30.00

characteristic of an unstable system. Though this phenomenon has been widely noted for non-linear flow few have attempted to investigate or explain it. Longuet-Higgins and Cokelet suggested it was due to the "physical growth of short gravity waves by horizontal compression of the crests of longer waves" [13] and proposed that these would be realistically damped by viscosity. They developed a five-point smoothing formula which takes advantage of the fact that alternate nodes on the free-surface form smooth curves and which is now widely used [34]. Moore [15] and Roberts [24] predicted that the instabilities were caused by a resonant interaction between the numerically induced discrete waves. They used linearised eigenvalue analysis techniques to prove that the removal of certain modes could stabilise the system.

In this paper we formulate a semi-discrete solution system to learn how the spatial discretisation affects the stability of linear gravity waves. The system evaluates a set of semi-discrete equations relating the temporal derivative of the discrete values of ϕ, the vector potential, and ζ, the surface elevation, and is of the form,

$$\begin{bmatrix} \phi_b \\ \zeta \end{bmatrix}_t = \mathbf{L} \begin{bmatrix} \phi_b \\ \zeta \end{bmatrix}, \tag{1}$$

where b indicates the values on the free-surface boundary, t represents differentiation in time, and $\mathbf{L}$ is a linear operator. Eigenvalues of $\mathbf{L}$ which contain a positive real component indicate an unstable system. An example of the dependency of the stability on the spatial discretisation is shown in Fig. 1 where several meshes are shown with their corresponding eigenvalues. The meshes (a) to (c) are all locally symmetric, that is, all the elements on the free-surface have a vertical line of symmetry, though not necessarily globally symmetric and have purely imaginary eigenvalues indicating stability, while the slightly asymmetric mesh d is unstable as it has positive real eigenvalues. Some mechanisms to recover a stable solution are then investigated and are used in conjunction with a revised arbitrary Lagrangian–Eulerian technique used by Ho [7] for spectral elements, and also widely used with finite element techniques [21], to solve non-linear free-surface flow.

In Section 2 we formulate the governing equations of a two-dimensional free-surface system, including boundary conditions for an arbitrary frame of reference. The *hp*/spectral element formulation to solve the system is also derived. Section 3 describes the eigenvalue stability analysis mentioned above and gives results of the eigenvalues and eigenvectors for varying spatial discretisations. It also puts forward a number of mechanisms to counter this instability. Results for the simulation of linear and non-linear free-surface flows are shown in Sections 4 and 5, respectively, along with error calculations and validation of our results. The conclusions to this work are given in Section 6.

2. INVISCID FREE-SURFACE GOVERNING EQUATIONS

We consider a Cartesian coordinate system, where the free-surface is described by $z = 0$, where z points vertically upwards and the free-surface height can be represented as $z = \zeta(x, t)$ as in Fig. 2.

As the fluid is irrotational, incompressible, and inviscid we can represent the velocity by the gradient of a potential such that

$$\mathbf{u} = \nabla\phi, \tag{2}$$

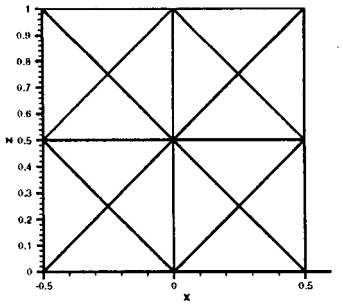

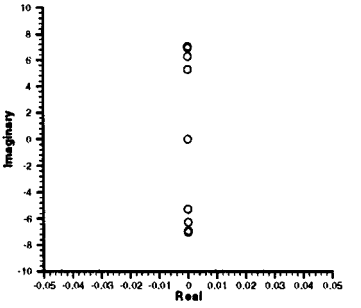

Mesh a

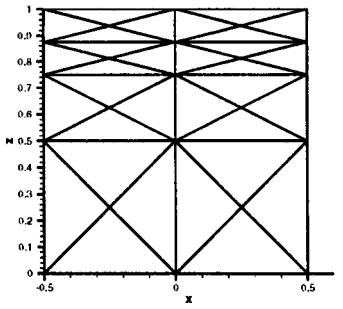

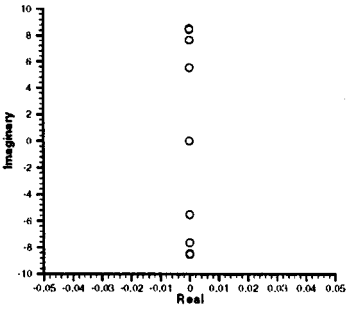

Mesh b

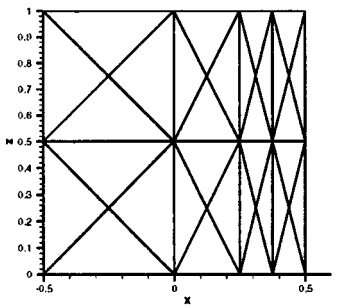

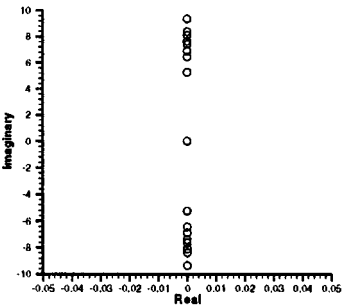

Mesh c

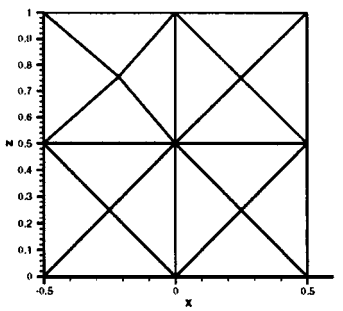

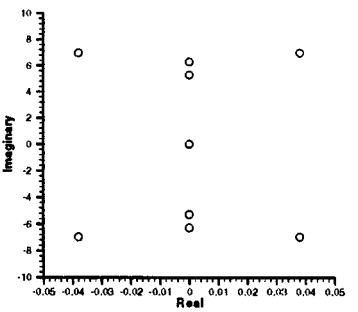

Mesh d

FIG. 1. Comparison of eigenvalues of spatially semi-discrete system for contrasting meshes.

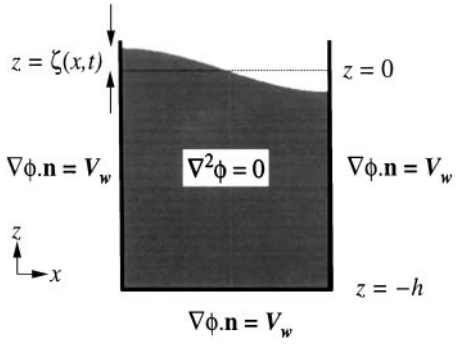

FIG. 2. Definition of frame of reference and wall boundary conditions for contained free-surface system.

and the system can be evaluated by solving the Laplacian

$$\nabla^2\phi = 0, \qquad \text{since } \nabla \cdot \mathbf{u} = 0, \tag{3}$$

supplemented by suitable boundary conditions.

2.1. *Boundary Conditions*

2.1.1. Eulerian boundary conditions. The Eulerian momentum equation for the inviscid free-surface is

$$\frac{\partial \mathbf{u}}{\partial t} + (\mathbf{u} \cdot \nabla)\mathbf{u} = -\frac{\nabla P}{\rho}, \tag{4}$$

and by substituting the following vector identity,

$$(\mathbf{u} \cdot \nabla)\mathbf{u} = \frac{1}{2}\nabla \mathbf{u}^2 - \mathbf{u} \times (\nabla \times \mathbf{u}), \tag{5}$$

into Eq. (4), while remembering $\nabla \times \mathbf{u} = 0$ for irrotational flow and $\mathbf{u} = \nabla\phi$, we are left with

$$\nabla \frac{\partial \phi}{\partial t} + \frac{1}{2}\nabla(\nabla\phi)^2 = -\frac{\nabla P}{\rho}. \tag{6}$$

By integrating spatially and substituting $P = \rho g \zeta$ (the excess pressure caused by a disturbance) where ζ describes the free-surface elevation and $z = \zeta(x, t)$, we have the non-linear Eulerian dynamic boundary condition,

$$\frac{\partial \phi}{\partial t} = -g\zeta - \frac{1}{2}\nabla\phi \cdot \nabla\phi. \tag{7}$$

The kinematic boundary condition is formulated by considering that a particle on the free-surface stays on the free-surface. Therefore

$$\frac{\partial \phi}{\partial z} = \frac{dz}{dt} \tag{8}$$

and using Eq. (2) combined with the material derivative identity for a stationary frame of reference,

$$\frac{df}{dt} = \frac{\partial f}{\partial t} + \mathbf{u} \cdot \nabla f, \tag{9}$$

where f is a spatially and temporally dependent function, we have the non-linear Eulerian kinematic boundary condition

$$\frac{\partial \phi}{\partial z} = \frac{\partial \zeta}{\partial t} + \frac{\partial \phi}{\partial x}\frac{\partial \zeta}{\partial x}. \tag{10}$$

2.1.2. Linearised boundary conditions. The standard linearised version of the Eulerian boundary conditions are obtained by considering small velocities ($\nabla\phi \ll 1$) and elevation ($\frac{\partial \zeta}{\partial x} \ll 1$) and ignoring any product of these. The resulting boundary conditions are therefore

$$\frac{\partial \phi}{\partial t} = -g\zeta, \tag{11}$$

$$\frac{\partial \phi}{\partial z} = \frac{\partial \zeta}{\partial t}, \tag{12}$$

which are evaluated on $z = 0$, or they can be combined to form one boundary condition for ϕ,

$$\frac{\partial^2 \phi}{\partial t^2} = -g\frac{\partial \phi}{\partial z}. \tag{13}$$

2.1.3. Boundary conditions in arbitrary reference frame. To change the frame of reference to an arbitrary one with velocity **w**, we substitute

$$\left.\frac{\partial \phi}{\partial t}\right|_{\mathbf{w}} = \frac{\partial \phi}{\partial t} + \mathbf{w}\cdot\nabla\phi, \tag{14}$$

into (7) and therefore have the dynamic boundary condition in an arbitrary frame of reference

$$\left.\frac{\partial \phi}{\partial t}\right|_{\mathbf{w}} = -g\zeta + \left(\mathbf{w} - \frac{1}{2}\nabla\phi\right)\cdot\nabla\phi. \tag{15}$$

In the same way we formulate the kinematic boundary condition in an arbitrary frame of reference to be

$$\left.\frac{\partial \phi}{\partial z}\right|_{\mathbf{w}} = \frac{\partial \zeta}{\partial t} + \left(\frac{\partial \phi}{\partial x} - w_x\right)\frac{\partial \zeta}{\partial x}, \tag{16}$$

where w_x is the x-component of **w**. Generally the frame of reference moves with the free-surface in the z direction and w_x is either zero or equal to $\frac{d\phi}{dx}$.

2.1.4. Wall boundary condition. The boundary conditions on the walls are such that

$$\nabla\phi\cdot\mathbf{n} = V_w, \tag{17}$$

where V_w represents the velocity at the wall.

2.2. *hp/Spectral Element Formulation*

To solve the system numerically we divide the two-dimensional fluid domain into finite elements and represent the velocity potential in terms of a set of modal expansions which vary with h, length of the elements, and p, the polynomial order of the function, and a corresponding set of coefficients. The velocity potential therefore takes the form

$$\phi \approx \phi^{\delta} = \sum_{i=1}^{ndof} \hat{\phi}_i N_i(x, y), \tag{18}$$

where ϕ is the exact solution, ϕ^{δ} is the numerical approximation, and the $\hat{\phi}_i$ are the coefficients of the modal expansion bases $N_i(x, y)$. To solve the Laplacian

$$\nabla^2 \phi = 0, \tag{19}$$

we first split ϕ into its constituent parts,

$$\nabla^2 \phi^H + \nabla^2 \phi^D = 0, \tag{20}$$

where ϕ^H represents the homogeneous value of the potential within the domain with zero Dirichlet boundary conditions, and ϕ^D are the known potential Dirichlet boundary conditions. We then construct the weak form of the equation by multiplying (20) by a test function, v^{δ}, and integrating over the domain. Following the Galerkin approach we set the test function to be of the same form as the approximation basis, i.e.,

$$v^{\delta} = \sum_{j=1}^{ndof} \hat{v}_j N_j(x, y), \tag{21}$$

where the symbols have the same meaning as above. Equation (20) then becomes

$$\int_{\Omega} \nabla^2 \phi^{H^{\delta}} \cdot v^{\delta} \, d\Omega + \int_{\Omega} \nabla^2 \phi^{D^{\delta}} \cdot v^{\delta} \, d\Omega = 0, \tag{22}$$

where Ω is the area of the domain. Utilising Green's Theorem the above equation becomes

$$-\int_{\Omega} \nabla \phi^{H^{\delta}} \cdot \nabla v^{\delta} \, d\Omega = \int_{\Omega} \nabla \phi^{D^{\delta}} \cdot \nabla v^{\delta} \, d\Omega - \int_{S} (\nabla \phi^{\delta} \cdot \mathbf{n}) v^{\delta} \, dS, \tag{23}$$

where S represents the boundary and $\mathbf{n}$ is the normal in the outward direction on the boundary. Denoting

$$\nabla \phi \cdot \mathbf{n} = \frac{\partial \phi}{\partial n}, \tag{24}$$

and by substituting in Eqs. (18) and (21) we are left with

$$-\int_{\Omega} \sum_{j=1}^{ndof} \hat{\phi}_i^H \nabla N_i \cdot \nabla N_j \, d\Omega = \int_{\Omega} \nabla \phi^D \cdot \nabla N_j \, d\Omega - \int_{S} \frac{d\phi^{\delta}}{dn} \cdot N_j \, dS \qquad \forall j, \tag{25}$$

where the $d\phi^S/\partial n$ are the Neumann boundary condition. In matrix form this can be written

as

$$\mathbf{L}\phi^H = \mathbf{f}, \tag{26}$$

where $\mathbf{L}$ and $\mathbf{f}$ are known and defined as

$$\mathbf{L}[i, j] = -\int_\Omega \nabla N_i \cdot \nabla N_j \, d\Omega, \tag{27}$$

$$\mathbf{f}[j] = \int_\Omega \nabla\phi^D \cdot \nabla N_j \, dA - \int_S \frac{d\phi^S}{\partial n} \cdot N_j \, dS, \tag{28}$$

and

$$\phi^H[i] = \hat{\phi}_i^H. \tag{29}$$

To solve for the unknowns we invert $\mathbf{L}$ and multiply through, i.e.,

$$\phi^H = \mathbf{L}^{-1}\mathbf{f}. \tag{30}$$

To evaluate the kinematic boundary condition we need to extract the velocity of the fluid, which requires taking the gradient of the velocity potential. A problem arises due to the modal basis being only C_0 continuous across elements and therefore the velocity and free-surface will be discontinuous. To recover the continuous velocity we follow a procedure set out in [34], which uses the Galerkin approach to evaluate a continuous velocity field, $\mathbf{d}$, over the whole domain, i.e.,

$$\int_\Omega \nabla\phi \cdot N_j \, d\Omega = \int_\Omega \sum_{i=1}^{ndof} \hat{d}_i N_i \cdot N_j \, d\Omega = \int_\Omega \mathbf{d} \cdot N_j \, d\Omega \qquad \forall j, \tag{31}$$

where $\int_\Omega N_i \cdot N_j \, d\Omega$ is the mass matrix. We used a modified version of the *hp*/spectral element $\mathcal{N}\varepsilon\kappa\mathcal{T}\,\boldsymbol{\alpha r}$ code [9, 25, 31, 32] to solve the free-surface flow. $\mathcal{N}\varepsilon\kappa\mathcal{T}\,\boldsymbol{\alpha r}$ is an *hp*/spectral element code utilising a hierarchal expansion basis of modified Jacobi polynomials of order p. A typical set of two-dimensional modal expansions for a polynomial of order 4 can be seen in Fig. 3.

The computations are performed on a mesh with elements of size h. Convergence can be achieved either by decreasing h or increasing p according to the theoretical error, presented

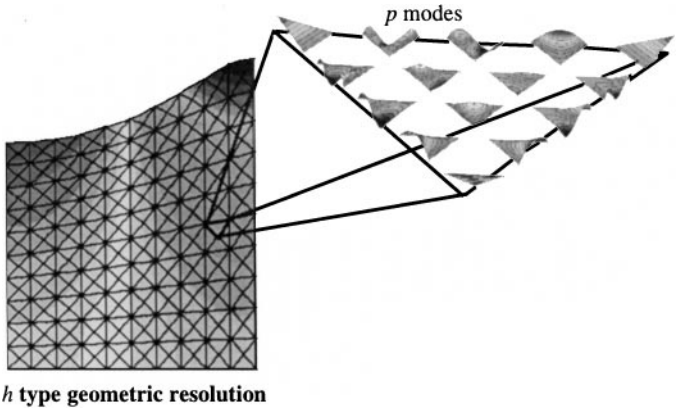

FIG. 3. Two-dimensional expansion modes up to polynomial order 4.

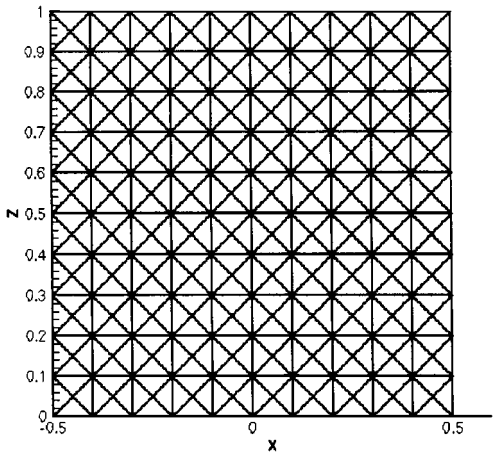

FIG. 4. Symmetric mesh for stability analysis.

by [28], of

$$\|u - u^{\delta}\|_{H^1(\Omega)} \leq Ch^{(\mu-1)} p^{(-k-1)} \|u\|_{H^k(\Omega)}, \tag{32}$$

where u is the exact value of the function, u^{δ} is the discretised approximated function, k is the differentiability of u, and $\mu = \min(k, p+1)$.

3. STABILITY ANALYSIS OF SPATIAL DISCRETISATION

We start our analysis by considering two basic mesh configurations; the first is a structured, symmetric mesh, shown in Fig. 4, and the second a structured, asymmetric mesh, shown in Fig. 5. We want to recognise the differences between the solutions for these different meshes in order to investigate how the computations were affected by the different

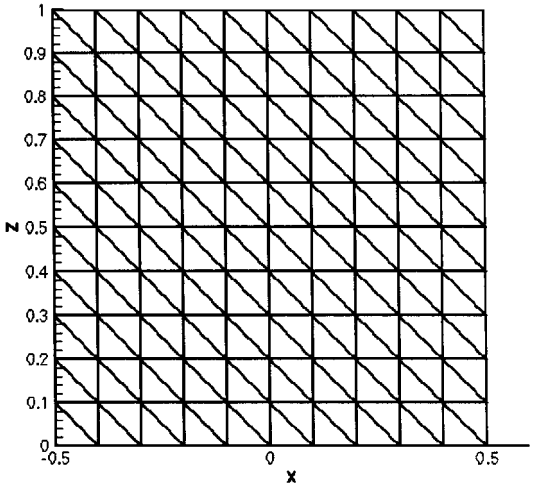

FIG. 5. Asymmetric mesh for stability analysis.

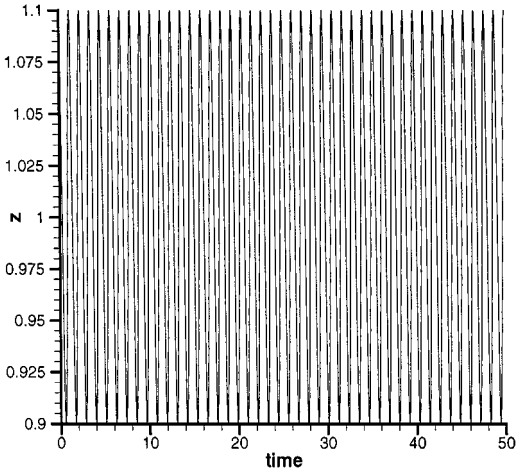

FIG. 6. Time history of point of maximum displacement.

spatial discretisations. The motivation to investigate asymmetric meshes comes from the wish to undertake non-linear flow solutions necessitating a moving mesh, which inevitably introduces distortion to the grid. We hypothesise that whatever numerical effect a distorted grid has on linear flow, it will have a similar effect on non-linear flow. All symmetric and asymmetric meshes used in this paper are of the same pattern as Figs. 4 and 5, respectively, and shall be denoted by the number of elements on each side i.e., Fig. 4 is a 10×10 symmetric mesh.

Using the *hp*/spectral element solver described in Section 3 the two meshes gave differing results for long time studies. The symmetric mesh was stable over long periods of time as shown in Fig. 6, where we see the time history of a point on the free-surface for over 50 time units at the point of maximum displacement.

The displacement, frequency, and wavelength are all constant and stability is achieved. Unfortunately the asymmetric mesh became unstable after relatively few periods. For initial conditions of $0.1\cos(\pi(x+0.5))$ the free-surface profiles for the symmetric and asymmetric mesh after approximately 2 periods is shown in Figs. 7 and 8, respectively.

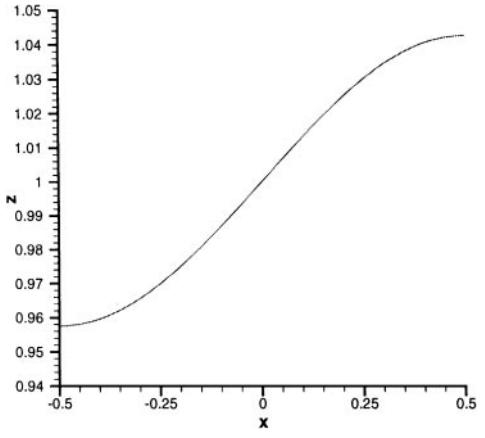

FIG. 7. Symmetric mesh free-surface profile at T = 1.14 s.

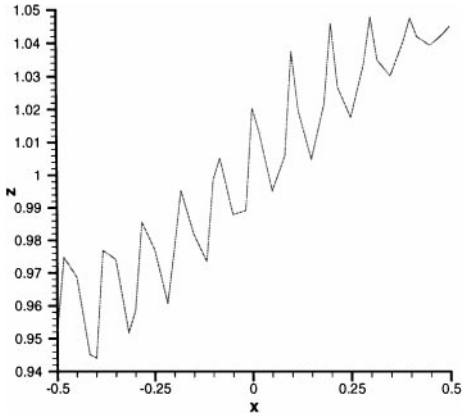

FIG. 8. Asymmetric mesh free-surface profile at T = 1.14 s.

The asymmetric mesh exhibits the familiar saw tooth pattern previously seen by many investigators [14].

Changing the type or order of the temporal discretisation merely changed the time step at which the computations became unstable. Decreasing the time step for any given temporal discretisation had no effect on the stability of the problem. We therefore decided to investigate the effect of the spatial discretisation by developing a semi-discrete formulation of the problem reduced to the solution values on the free-surface boundary.

3.1. *Formulation of Semi-discrete Eigenvalue and Eigenvector Analysis*

In order to formulate a semi-discrete system to investigate the stability of the numerical problem we decompose the Laplacian into its interior and free-surface boundary components, i.e.,

$$\mathbf{L}\phi = \begin{bmatrix} \mathbf{L}_{ii} & \mathbf{L}_{ib} \\ \mathbf{L}_{bi} & \mathbf{L}_{bb} \end{bmatrix} \begin{bmatrix} \phi_i \\ \phi_b \end{bmatrix} = \mathbf{0}, \tag{33}$$

where the subscript b refers to the degrees of freedom on the free-surface boundary and i refers to all remaining degrees of freedom. The first row of this system can be rearranged to obtain

$$\mathbf{L}_{ii}\phi_i + \mathbf{L}_{ib}\phi_b = \mathbf{0} \Rightarrow \phi_i = -\mathbf{L}_{ii}^{-1}\mathbf{L}_{ib}\phi_b. \tag{34}$$

Equation (34) therefore expresses the interior degrees of freedom in terms of the free-surface boundary degrees of freedom. This is possible due to the elliptic nature of the Laplace equation. The differential of ϕ in the z-direction can similarly be represented by an operator $\mathbf{D}$ such that

$$\mathbf{D}\phi = \begin{bmatrix} \mathbf{D}_{ii} & \mathbf{D}_{ib} \\ \mathbf{D}_{bi} & \mathbf{D}_{bb} \end{bmatrix} \begin{bmatrix} \phi_i \\ \phi_b \end{bmatrix}. \tag{35}$$

Considering the bottom line of Eq. (35) we find an expression for the differential on the boundary to be

$$\left.\frac{\partial \phi}{\partial \boldsymbol{z}}\right|_b = \mathbf{D}_{bi}\phi_i + \mathbf{D}_{bb}\phi_b. \tag{36}$$

where $\frac{\partial \phi}{\partial \boldsymbol{z}}|_b$ is a vector of the values of $\frac{\partial \phi}{\partial \boldsymbol{z}}$ on the free-surface. Substituting (34) into (36) we obtain a relationship for the differential in terms of the boundary values of the velocity potential, i.e.,

$$\left.\frac{\partial \phi}{\partial \boldsymbol{z}}\right|_b = -\mathbf{D}_{bi}\mathbf{L}_{ii}^{-1}\mathbf{L}_{ib}\phi_b + \mathbf{D}_{bb}\phi_b = \left[\mathbf{D}_{bb} - \mathbf{D}_{bi}\mathbf{L}_{ii}^{-1}\mathbf{L}_{ib}\right]\phi_b = \boldsymbol{N}_{\mathbf{D}}\phi_b, \tag{37}$$

where $\boldsymbol{N_D}$ can be thought of as a discrete Dirichlet–Neumann operator. By combining (37) with the linear free-surface boundary conditions

$$\frac{\partial \phi}{\partial t} = -g\zeta, \tag{38}$$

$$\frac{\partial \phi}{\partial z} = \frac{\partial \zeta}{\partial t}, \tag{39}$$

we can now form the semi-discrete form of the linear free-surface movement

$$\begin{bmatrix} \phi_b \\ \zeta \end{bmatrix}_t = \begin{bmatrix} \mathbf{0} & -g\boldsymbol{I} \\ \boldsymbol{N}_{\mathbf{D}} & \mathbf{0} \end{bmatrix} \begin{bmatrix} \phi_b \\ \zeta \end{bmatrix}. \tag{40}$$

The eigenvalues of the operating matrix dictate the stability of the scheme which implies that we must find the eigenvalues, s_n, such that

$$\begin{bmatrix} \mathbf{0} & -g\boldsymbol{I} \\ \boldsymbol{N_D} & \mathbf{0} \end{bmatrix} \begin{bmatrix} \psi_n \\ \eta_n \end{bmatrix} = s_n \begin{bmatrix} \psi_n \\ \eta_n \end{bmatrix}, \tag{41}$$

where $\boldsymbol{\psi_n}$ and $\boldsymbol{\eta_n}$ denote the eigenvectors. This system can be rearranged to form

$$-s_n\boldsymbol{\psi}_n - g\boldsymbol{\eta}_n = \mathbf{0}, \tag{42}$$

$$\boldsymbol{N}_D\boldsymbol{\psi}_n - s_n\boldsymbol{\eta}_n = \mathbf{0}, \tag{43}$$

and substituting Eq. (42) into Eq. (43) we obtain an equation for the eigenvalues of the full matrix in terms of those of the Neumann–Dirichlet operator matrix,

$$s_n^2\boldsymbol{I}\boldsymbol{\eta}_n + g\boldsymbol{N_D}\boldsymbol{\eta}_n = \mathbf{0}. \tag{44}$$

If we denote the eigenvalues and eigenvectors of $\boldsymbol{N_D}$ by μ_n and $\boldsymbol{\alpha}_n$, respectively, i.e.,

$$\boldsymbol{N_D}\boldsymbol{\alpha}_n = \mu_n\boldsymbol{\alpha}_n, \tag{45}$$

where μ_n is complex, then we obtain

$$s_n^2 = -\mu_n g, \tag{46}$$

or

$$s_n = \pm i(\mu_n g)^{\frac{1}{2}}. \tag{47}$$

Therefore if we consider the general form of μ_n, stating its phase and magnitude,

$$\mu_n = |\mu_n| e^{i\theta}, \tag{48}$$

then

$$s_n = \pm i g^{\frac{1}{2}} |\mu_n|^{\frac{1}{2}} e^{i\frac{\theta}{2}} \tag{49}$$

$$= \pm g^{\frac{1}{2}} |\mu_n|^{\frac{1}{2}} e^{i(\frac{\theta}{2}+\frac{\pi}{2})}. \tag{50}$$

If $\theta = 0$ then μ_n is real and we have purely imaginary s_n eigenvalues, and the matrix system (40) will have a purely dispersive solution. If $\theta \neq 0$ then the eigenvalues, s_n, have a positive and negative real component resulting in an unstable system. For stability of an inviscid, incompressible linear free-surface flow we require the eigenvalues of the matrix to be purely imaginary. We can then conclude that any imaginary component in μ_n leads to instability, caused by an asymmetry in the x-direction of the computational mesh.

3.1.1. Validation of numerical implementation. We measure the accuracy of the numerical implementation by comparing the analytical values of the system's eigenvalues with the eigenvalues of the numerical system. System (40) can be represented analytically by

$$\begin{bmatrix} \phi_b \\ \zeta \end{bmatrix}_t = \begin{bmatrix} \mathbf{0} & -g\boldsymbol{I} \\ k\tanh(kh) & \mathbf{0} \end{bmatrix} \begin{bmatrix} \phi_b \\ \zeta \end{bmatrix}, \tag{51}$$

where k is the wavenumber and h the height of the free-surface. The resulting eigenvalues of this system are therefore

$$\lambda = \pm(gk\tanh(kh))^{\frac{1}{2}} i. \tag{52}$$

The first analytical eigenvalue is represented by $k = \pi$ and has a value of $\lambda_1 = \pm 5.541131i$. Figure 9 shows the plot of the error, ε, between this analytical value and that produced

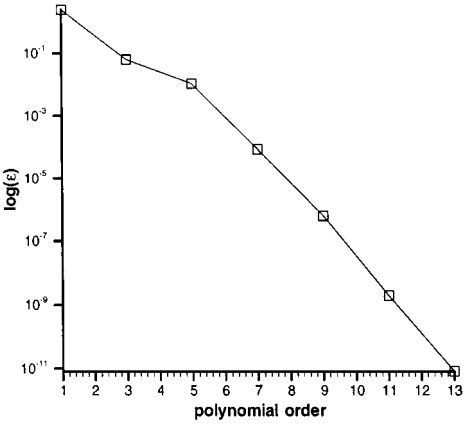

FIG. 9. First eigenvalue error for varying polynomial order, p.

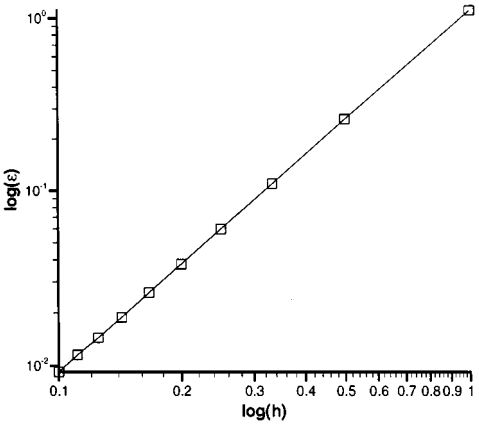

FIG. 10. First eigenvalue error for varying element size, h.

computationally on a 2×2 symmetric mesh as the order of the expansions, p, increases and Fig. 10 shows the error as the size of the elements, h, decreases for similar shaped symmetric meshes. Figure 9 shows that $\log(\varepsilon)$ is proportional to p and Fig. 10 that $\log(\varepsilon) \propto \log(h)$ proving standard *hp* convergence.

3.2. *Spatial Discretisation Comparison*

To illustrate the above analysis we consider the case of 10×10 symmetric and asymmetric meshes. The spectral analysis was undertaken with $p = 2$ and the corresponding eigenvalues and eigenvectors can be seen in Figs. 11–12. In Fig. 11 we see the eigenspectrum for the symmetric and asymmetric meshes. The symmetric eigenspectrum clearly indicates a stable solution while the solution for the asymmetric mesh is unstable. The first three corresponding eigenvectors in terms of ζ are shown in Fig. 12. We note the sinusoidal form of the eigenvectors corresponding to the analytical solution. The asymmetric mesh, however, leads to a set of asymmetric eigenvectors biased in the same direction as the free-surface elements of the asymmetric mesh.

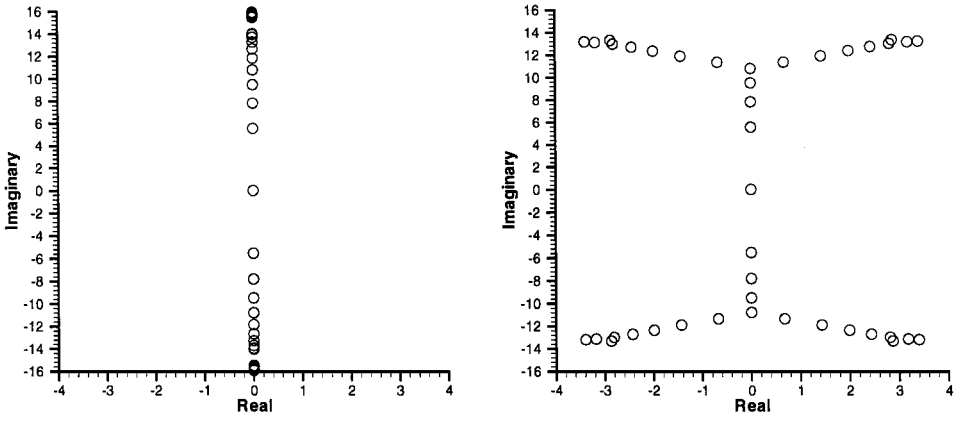

FIG. 11. Eigenvalues indicating stability for symmetric mesh (left) and eigenvalues indicating instability for asymmetric mesh.

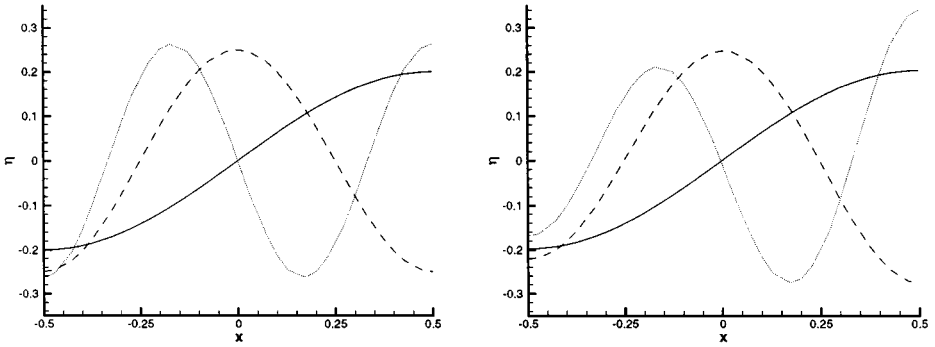

FIG. 12. First three eigenvectors in terms of frequency for symmetric (left) and asymmetric mesh.

3.3. *Mechanisms for Stability*

We have seen that symmetric and deformed meshes play an important part in free-surface computations therefore we need a mechanism to numerically enforce the stability of the computations.

3.3.1. Removal of high modes. We follow a procedure proposed by both Moore [15] and Roberts [24], who theorised that the incorrect phase relation of the discretised system leads to a resonance with the lower frequency causing the instability for the non-linear problem. To remove the instability they removed the higher modes and in *hp* methods we can apply a similar technique. The higher modes are simply removed by zeroing the coefficients of the highest frequency modal shape functions. Figure 14 shows the resulting purely imaginary eigenvalues for computations using polynomial order 2 with the removal of the highest mode after differentiation. Compare this to Fig. 13 which shows the eigenvalues with no removal of modes.

Unfortunately as the original polynomial order increases more modes have to be removed to enforce stability resulting in very expensive calculations for high accuracy solutions.

3.3.2. Addition of a diffusive term. Artificial diffusion is commonly used in compressible flow simulation to remove numerical instabilities and is attractive in finite element methods due to the ease with which it can be implemented. To this end we consider adding

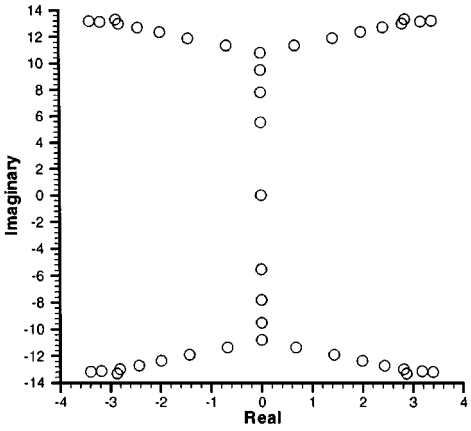

FIG. 13. Eigenvalues for asymmetric mesh with no mode removal.

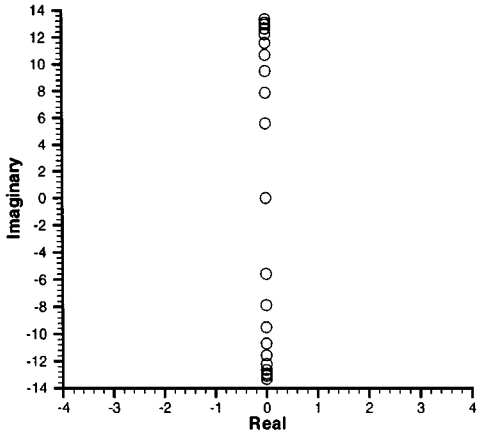

FIG. 14. Eigenvalues for asymmetric mesh with removal of highest mode.

a diffusive term to the kinematic boundary condition to enforce stability. The kinematic boundary condition then becomes

$$\frac{\partial \zeta}{\partial t} = \frac{\partial \phi}{\partial z} + \mu \frac{\partial^2 \zeta}{\partial x^2}, \tag{53}$$

where μ is a constant dependent upon the discretisation properties $(h,\ p)$. We denote μ_{critical} or μ_c as the lowest value of μ which produces a stable solution. This added term has the benefit of diffusing high frequency displacements of the free-surface, i.e., the saw-tooth effect, but unfortunately also damps the entire system. The resulting eigenvalues of the semi-discrete system with a polynomial expansion basis of order 2 and $\mu_c = 3 \times 10^{-4}$ evaluated on an asymmetric mesh (Fig. 5) are shown in Fig. 15. All the real parts are non-positive indicating stability.

Before we can assess the relationship between μ_c, h, p, and the asymmetry of the mesh, we must first mathematically quantify the meaning of mesh asymmetry or skewness. We represent the size of an element by h, the length of the element's side on the free-surface. We also need to formulate a characteristic length representing the amount of skewness of an element. Figure 19 shows a typical skewed element illustrating the length σ which

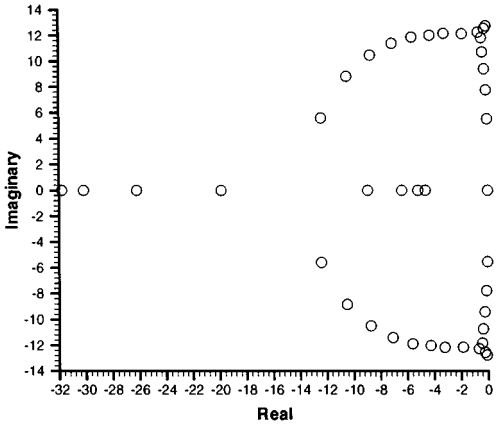

FIG. 15. Eigenvalues for asymmetric mesh with added diffusion term.

represents the salient asymmetry of our problem. We denote line AB as the vertical unit vector, $\boldsymbol{e_z}$, and the line CD as the intercept of the centre of the element's free-surface side and its interior vertex. The angle θ is the angle between these two lines. If the coordinates of the vertices are denoted by X_1, X_1, and X_3, where $X_j = (x_j, y_j)$ then

$$\boldsymbol{AB} = \boldsymbol{e_z} \tag{54}$$

$$\boldsymbol{CD} = \left[x_3 - \left(\frac{x_1 + x_2}{2}\right)\right]\boldsymbol{e_x} + \left[y_3 - \left(\frac{y_1 + y_2}{2}\right)\right]\boldsymbol{e_z}, \tag{55}$$

and

$$|\mathbf{CD}| \sin\theta = \frac{\mathbf{AB} \times \mathbf{CD}}{|\mathbf{AB}|}. \tag{56}$$

We can therefore represent the characteristic length of the skewness of an element, σ, as

$$\sigma = \mathbf{AB} \times \mathbf{CD} \tag{57}$$

and the non-dimensionalised skewness of an element, κ, as

$$\kappa = \frac{\sigma}{h}. \tag{58}$$

Figure 16 shows the values of μ_c for varying values of σ. When $\sigma = 0$ we have an symmetric mesh and as σ increases the asymmetry of the mesh increases, as does μ_c. It can be seen that the data almost collapses to a single curve purely dependent on σ. It must be remembered that although the figure seems to indicate non-dependency on h, for similar shaped meshes, h and σ are proportional, i.e., $\kappa =$ constant. We believe the dependence of the solution's stability on the skewness of an element, with respect to the vertical, comes from the dependence of the kinematic boundary condition on the accurate solution of $\frac{\delta\phi}{\delta z}$. A largely skewed element will not accurately evaluate this derivative for at least one of its free-surface vertices. Figure 17 shows the value of μ_c for increasing values of p performed on 1×1, 2×2, and 4×4 asymmetric meshes corresponding to element sizes $h = 1.0$, $h = 0.5$, and $h = 0.25$. μ_c was evaluated by finding the lowest possible value of μ, to 8 decimal places, which gave purely

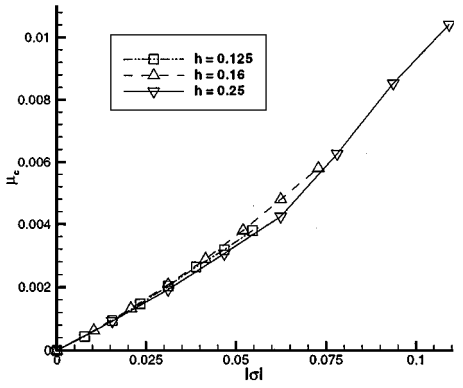

FIG. 16. μ_c for increasing σ and varying h with $p = 2$.

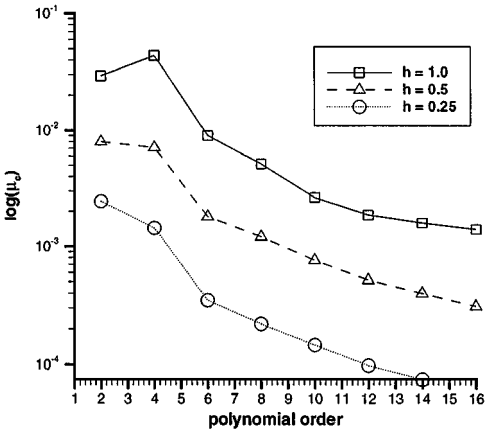

FIG. 17. μ_c for varying order of expansion basis where h represents the size of the element edge on the free-surface.

imaginary eigenvalues. A relationship of the form $\log(\mu_c) \propto p$ is apparent. We therefore hypothesise that the relationship is of the form

$$\mu_c = C\sigma^{\alpha p}, \tag{59}$$

where α and C are positive constants. To test this theory we measured the value of μ_c for increasing σ on a 5×5 mesh for differing values of p. The results are shown in Fig. 18 and support our hypothesis as $\log(\mu_c) \propto \log(|\sigma|)$ with the steepness of the lines increasing with p. By utilising the information contained in Figs. 17 and 18, μ_c can be numerically bounded by taking C as $\frac{1}{10}$ and α as 0.2. Equation (59) is consistent with the requirement that $\mu_c \to 0$ upon convergence. Further more it is consistent with the *hp* spectral element approximation such that μ_c should decay as $h^{\alpha p}$ as σ is proportional to h for different sizes of similar shaped elements.

This procedure is only valid if the accuracy of the solution behaves identically as before, i.e., $\epsilon \propto h^p$. The numerical validation of this can be seen in Figs. 21 and 22 where the error of the first eigenvalue is plotted against increasing p and h, respectively. In Fig. 21 mesh a

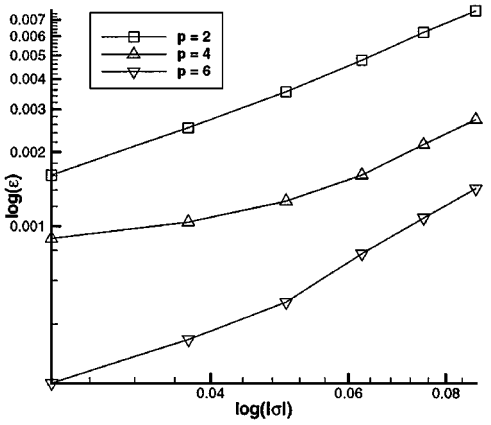

FIG. 18. μ_c for increasing σ and varying p with $h = 0.2$.

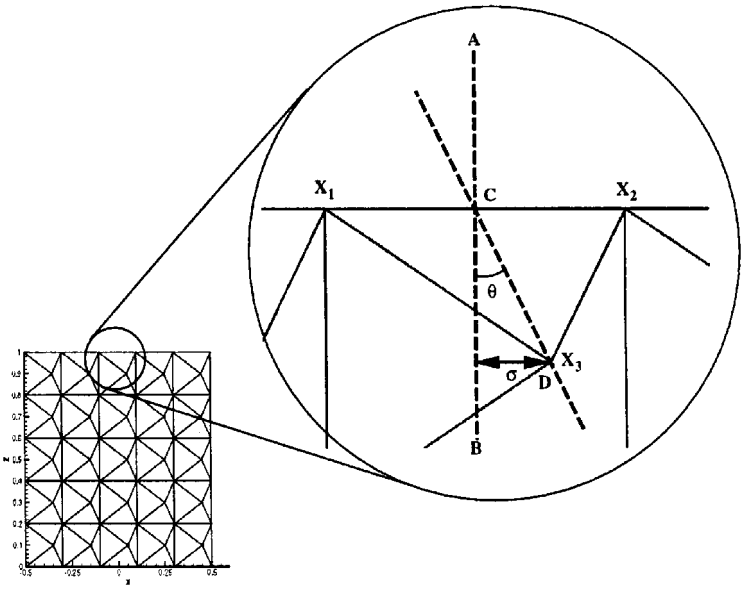

FIG. 19. Diffusion coefficient is dependent on the distance σ.

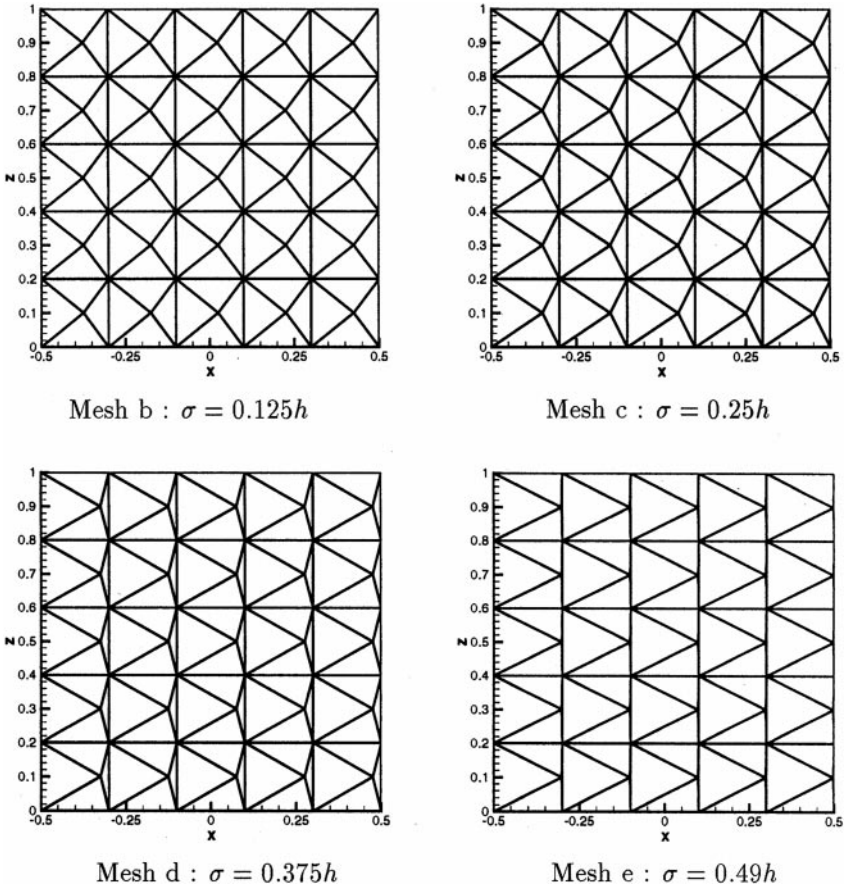

FIG. 20. Meshes used for first eigenvalue error analysis.

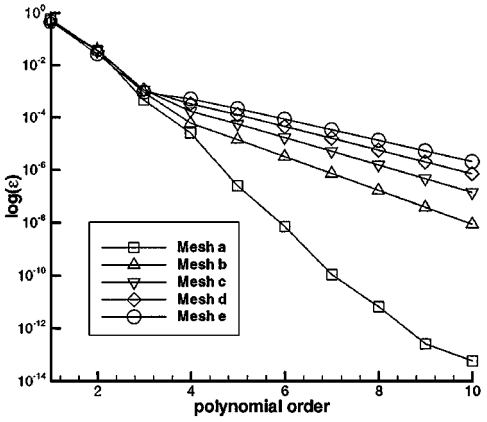

FIG. 21. First eigenvalue error for varying order of expansion basis for $h = 0.2$.

is a 5×5 symmetric mesh while meshes b to e refer to those in Fig. 20. Figure 22 illustrates the rate of convergence, which is consistent with *hp* convergence, i.e., $\log(\varepsilon) \propto \log(h)$. It can be seen in both figures that the rate of convergence is proportional to the skewness of the mesh, with a distorted mesh undergoing slower convergence.

4. LINEAR FREE-SURFACE FLOW

Having developed a stability enforcing mechanism we investigate the accuracy of our unsteady code. A 10×10 symmetrical mesh was used (Fig. 23) for the computations and the error was evaluated by comparing the computational results with the theoretical solution

$$\phi = A \cosh(ky) \cos(\omega t) \cos(kx), \tag{60}$$

where h is the height of the free-surface, k is the wavenumber, ω is the frequency of the oscillations, and

$$\omega^2 = gk \tanh(k). \tag{61}$$

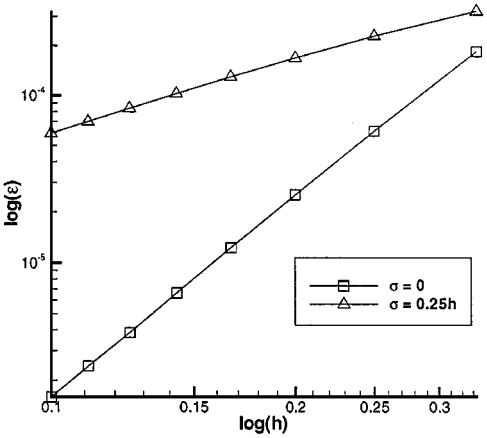

FIG. 22. First eigenvalue error for varying order of element size for $p = 4$.

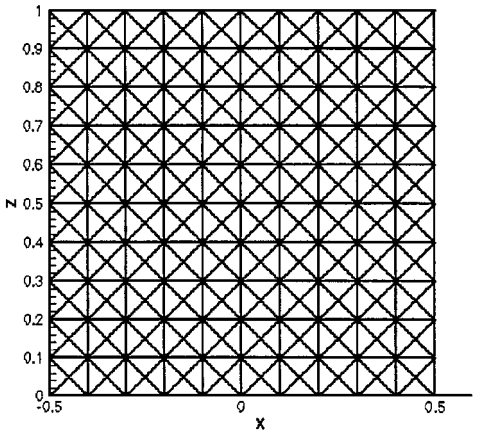

FIG. 23. Symmetric mesh used for linear free-surface computations.

The initial conditions were

$$\zeta = 0 \tag{62}$$

and

$$\phi = A\cosh(ky)\cos(kx) \qquad \text{on } z = 0, \tag{63}$$

where A determines the amplitude of the free-surface motion. In Fig. 24 we see the time-history of a particle on the free-surface which experiences the maximum displacement for increasing order of expansion basis. The initial condition was $k = \pi$ and A was chosen so that the maximum displacement is approximately 0.1, as shown in Fig. 24.

The phase error when $p = 1$, i.e., when we are using a linear expansion basis, can clearly be seen in Fig. 24, as can the rapid convergence of the computation when the order of the basis increases; $p = 3$ and $p = 5$ are indistinguishable from each other. The $\mathbf{H}^1$ error plots shown in Figs. 25 and 26 demonstrate that $\log(\varepsilon) \propto p$ and $\log(\varepsilon) \approx 2\log(\Delta t)$ as expected since we used a second order time integration scheme to discretise the combined linear

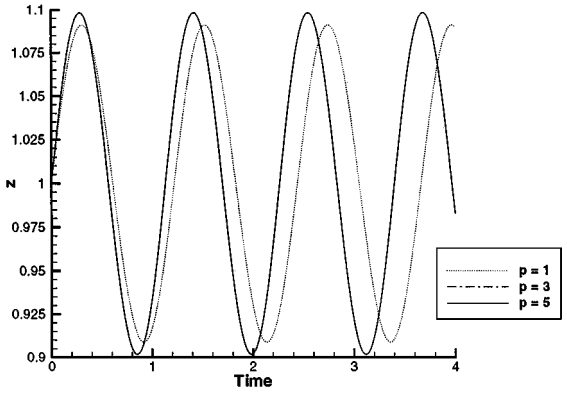

FIG. 24. Time history of particle for linear flow.

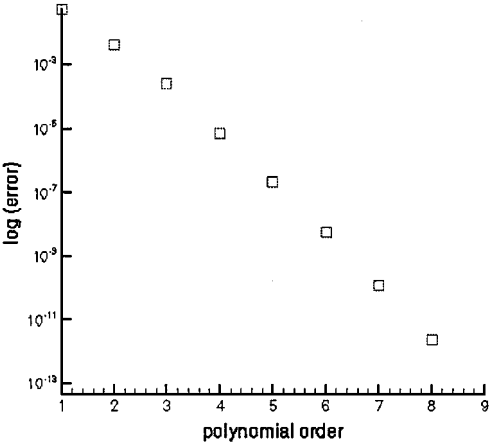

FIG. 25. Error convergence for increasing polynomial order.

boundary condition (13) such that

$$\frac{\phi^{n+1} - 2\phi^n + \phi^{n-1}}{\Delta t^2} = -g\frac{\partial z}{\partial \phi}. \tag{64}$$

5. NON-LINEAR FREE-SURFACE FLOW

The non-linear flow was numerically simulated using a fully Lagrangian version of the dynamic and kinematic boundary conditions, i.e.,

$$\frac{d\phi}{dt} = -gz + \frac{1}{2}\nabla\phi \cdot \nabla\phi, \tag{65}$$

$$\frac{\partial \phi}{\partial x} = \frac{dx}{dt}, \tag{66}$$

$$\frac{\partial \phi}{\partial z} = \frac{dz}{dt}. \tag{67}$$

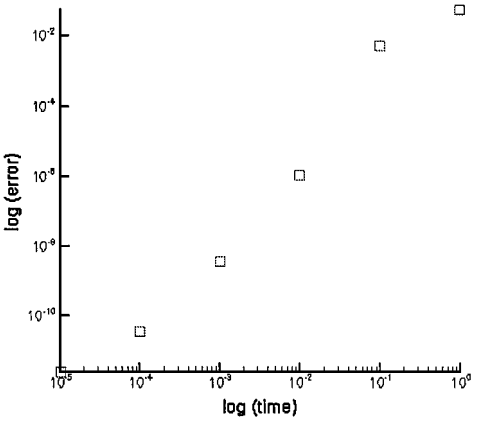

FIG. 26. Error convergence for decreasing Δt.

To enforce stability we introduce a diffusive term into the kinematic boundary condition,

$$\frac{dz}{dt} = \frac{\partial \phi}{\partial z} + \mu \frac{\partial^2 z}{\partial x^2}. \tag{68}$$

The mesh must be updated each time step so that it contains the entire fluid domain. We ensure this by solving two Laplacian equations of the form

$$\nabla^2 x = 0, \tag{69}$$

$$\nabla^2 z = 0, \tag{70}$$

where the Dirichlet boundary conditions were applied using the x and y values of the nodal points on the boundary. The nodal points on the free-surface were obtained from the Lagrangian motion of the fluid. The side wall nodal points are then linearly adjusted according to the motion of the fluid when in comes into contact with the walls, while the bottom walls nodes are stationary. To ensure the accuracy of the model we test our computational results against other analytical and computational results.

The first comparison is made with second order analytical results developed by Wu and Eatock Taylor [34]. An equation is formulated to calculate the value of ζ at any time for sloshing in a rectangular box. The computations were performed for a box of length 2 and depth 1 with an initial maximum displacement of 0.1 and polynomial order 2. The mesh in its initial state is shown in Fig. 27 and the comparison between the analytical and computational results shown in Fig. 28.

The two results are in good agreement and as Wu and Eatock Taylor suggest the discrepancies can be attributed to the fact that the analytical results are only second order, while the computations take into consideration higher order effects. The non-linear wave profile of this motion can be seen in Fig. 29.

The next comparison is between qualitative analytical data derived by Wu [33]. The results concern a submerged cylinder undergoing sinusoidal horizontal and vertical motion. He hypothesises that the frequency of the vertical force on a submerged cylinder undergoing horizontal motion is twice that of the horizontal force. The domain was meshed using a finite element meshing code called **FELISA** [18, 19]; a close up of the mesh around the

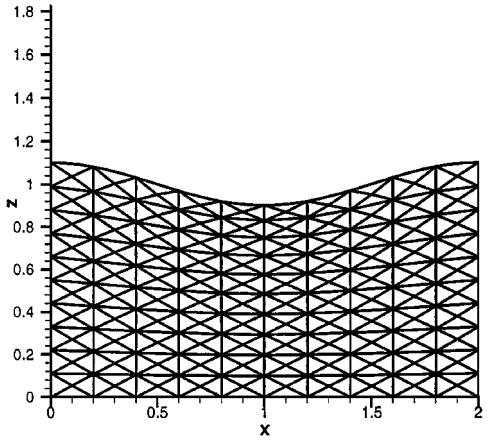

FIG. 27. Initial conditions and mesh used for non-linear sloshing.

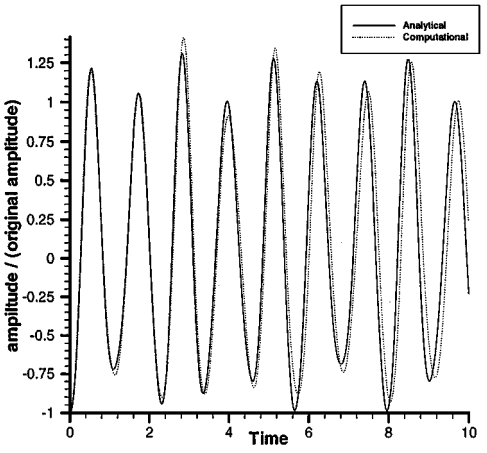

FIG. 28. Computational and analytical time history of particle for non-linear flow.

cylinder can be seen in Fig. 31. The domain is 100 units in length and 2 in depth. The radius of the cylinder is $r = 0.5$ and its centre is submerged by 0.75, identical to the setup used in [35]. The maximum displacement is $\frac{r}{2}$ and the wave-frequency was 1. Figure 30 illustrates the frequency doubling and Fig. 32 shows the free surface profile at time $T = 3$ and $T = 9$.

Further correlation is sought by investigating wave motion contained within a box which is undergoing sinusoidal translational motion. Faltinsen [3] formulated a linear solution for this motion and we use the same case studies in Wu *et al.* [36] to test the computations. The free-surface position, ζ, is calculated using

$$\zeta = \zeta_1 + \zeta_2, \tag{71}$$

where

$$\zeta_1 = \frac{a}{g}\left(x\omega^2 + \sum_{n=0}^{\infty} C_n \omega \sin k_n x\right) \sin \omega t \tag{72}$$

$$\zeta_2 = -\frac{a}{g}\sum_{n=0}^{\infty} \omega_n \left(C_n + \frac{H_n}{\omega^2}\right) \sin k_n x \sin \omega_n t \tag{73}$$

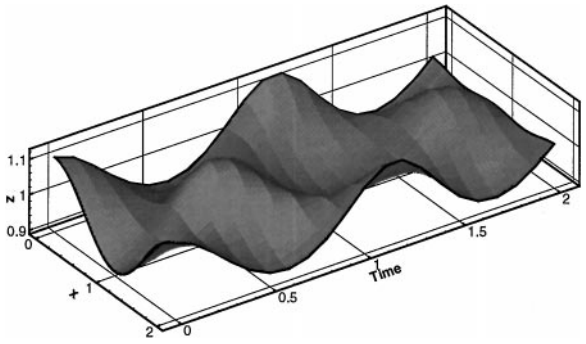

FIG. 29. Time history of fluid surface for Lagrangian flow for comparison with Wu and Eatock Taylor's analytical scheme with $p = 3$.

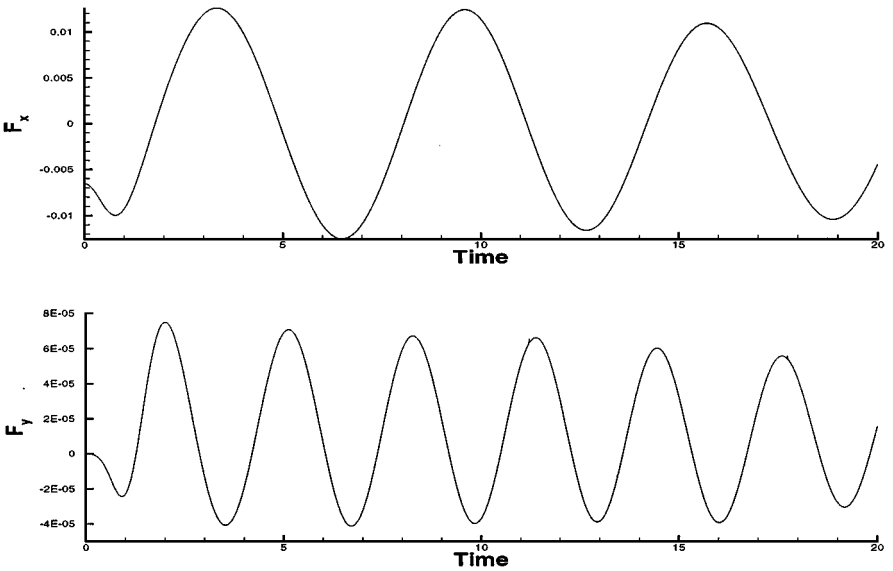

FIG. 30. Horizontal force (above) and vertical force on a submerged cylinder undergoing horizontal oscillations close to a free-surface.

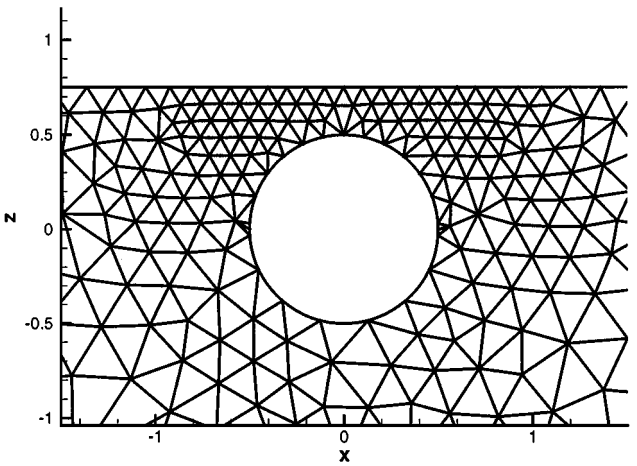

FIG. 31. Computational domain for horizontally oscillating cylinder at T = 0. Note the use of symmetric triangular elements on the free-surface.

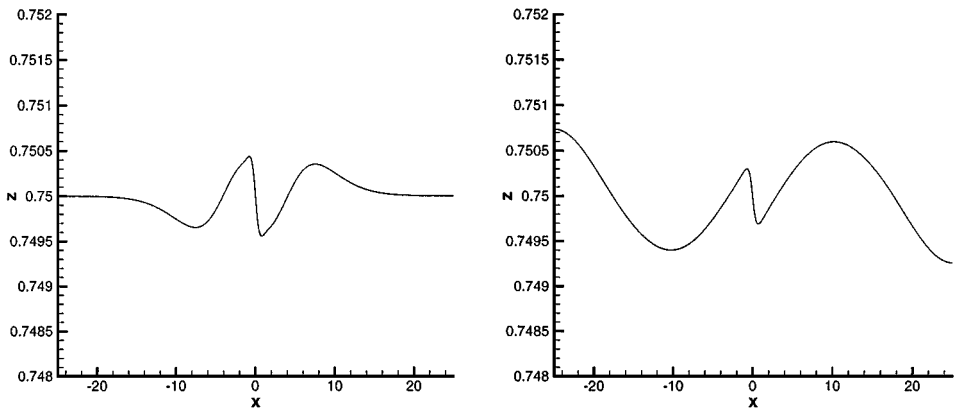

FIG. 32. Free-surface disturbance due to a horizontally oscillating submerged cylinder at T = 3 (left) and T = 9.

and

$$k_n = \frac{2n+1}{L}\pi \tag{74}$$

$$\omega_n^2 = gk_n \tanh k_n d \tag{75}$$

$$H_n = \omega^3 \frac{4}{L}\frac{(-1)^n}{k_n^2} \tag{76}$$

$$C_n = \frac{H_n}{\omega_n^2 - \omega^2}. \tag{77}$$

L and d are the length and breadth of the tank and are both 1. ω is the wave frequency of the forced oscillations which are described by

$$x = a\cos\omega t, \tag{78}$$

where a is 0.002 so the motion is largely linear. The computations were undertaken on a 10×10 symmetric mesh.

The ω_n are the natural frequencies of the motion and if ω is equal to one of them the displacement will reach infinity. The motion is primarily driven by the first natural frequency, ω_0, and the driven frequency, ω. The difference between these frequencies defines the wave envelope. We attempted four simulations, one for $\omega = 0.5414\omega_0$, $\omega = 0.9\omega_0$, $\omega = 1.1\omega_0$, and $\omega = 0.999\omega_0$. Figure 33 shows the analytical and computational results for $\omega = 0.5414\omega_0$ and very good agreement is seen. Figures 34 and 35 are close to the resonant frequency and therefore the amplitude of the wave grows much larger. Agreement is still very good especially close to start up, though as the amplitude grows non-linear characteristics of higher peaks and troughs are shown by the computational results, which are missed be the linear analysis. These effects are even more apparent in Fig. 36 where the forcing frequency is almost identical to the first natural frequency and the amplitude increases greatly.

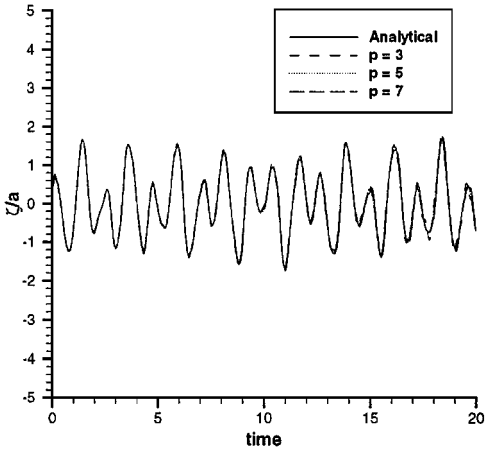

FIG. 33. $\omega = 0.5414\omega_0$.

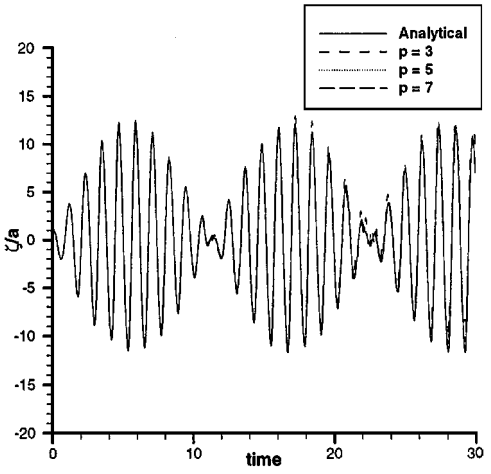

FIG. 34. $\omega = 0.9\omega_0$.

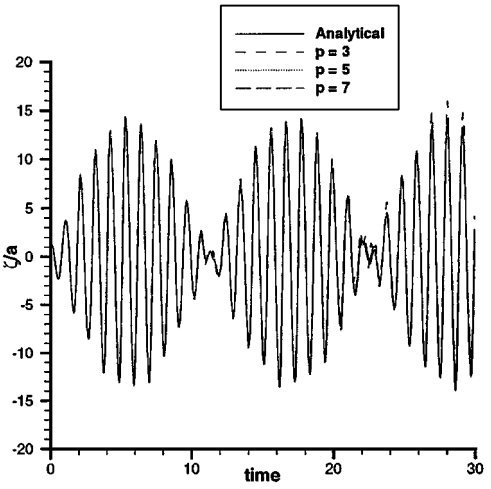

FIG. 35. $\omega = 1.1\omega_0$.

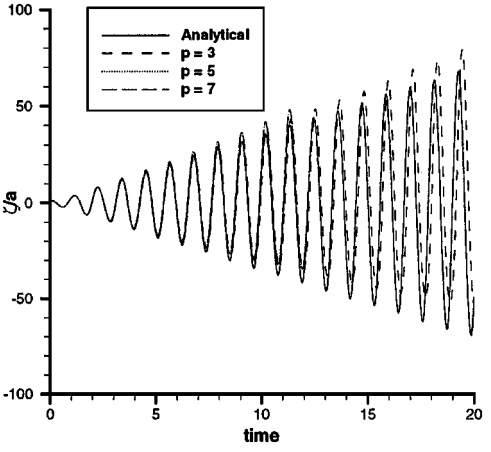

FIG. 36. $\omega = 0.999\omega_0$.

6. CONCLUSIONS

In this paper we have computationally simulated linear and non-linear free-surface flows using an *hp*/spectral technique. A semi-discrete system was formulated to investigate the stability of the spatial discretisation used in the linear computations. It was found that an asymmetric mesh was inherently unstable, while a symmetric mesh was stable and that this instability was attributed to the dispersive nature of the discrete Neumann–Dirichlet operator associated with the asymmetric mesh. Mechanisms to enforce stability were defined and tested and investigation suggested that the addition of a diffusive term in the kinematic boundary condition, where the coefficient is consistent with the *hp*/spectral approach and takes into account the skewness of the mesh with regard to the symmetry of local elements, was suitable. These findings were then used to simulate non-linear free-surface flow for different conditions. The results were validated by comparing them to qualitative and quantitative results for sloshing, translational movement of a submerged cylinder, and for translational forced oscillations of the containing tank. Future work will involve the investigation of viscous free-surface flows.

ACKNOWLEDGMENTS

This work was undertaken under the sponsorship of EPSRC. We also thank Professor Graham from Imperial College for his valuable help and Tim Warburton for providing the initial code.

REFERENCES

1. X. Cai, H. P. Langtangen, B. F. Neilsen, and A. Tveito, A finite element method for fully nonlinear water waves, *J. Comput. Phys.* **143**, 544 (1998).
2. D. G. Dommermuth and D. K. P. Yue, A high-order spectral method for the study of non-linear gravity waves, *J. Fluid Mech.* **184**, 267 (1987).
3. O. M. Faltinsen, A numerical non-linear method of sloshing in tanks with two dimensional flow, *J. Ship Res.* **18**(4), 224 (1978).
4. D. Gottlieb and S. A. Orszag, *Numerical Analysis of Spectral Methods: Theory and Applications* (Soc. for Industr. & Appl. Math. Philadelphia, 1977).
5. R. D. Henderson and G. E. Karniadakis, Unstructured spectral element methods for the incompressible navier–stokes equations, in *Finite Elements in Fluids* (CIMNE/Pineridge, Swansea, 1993).
6. C. Hirsch, *Numerical Computation of Internal and External Flows* (Wiley, New York, 1988).
7. L.-W. Ho, *A Legrende Spectral Element Method for Simulation of Incompressible Free-Surface Flows*, Ph.D. thesis, Massachustts Institute of Technology, 1989.
8. A. Huerta and L. Wing Kam, Viscous flow with large free surface motion, *Comput. Methods Appl. Mech. Eng.* **69**, 277 (1988).
9. G. E. Karniadakis and S. J. Sherwin, *Spectral/hp Element Methods for CFD* (Oxford Univ. Press, London, 1999).
10. D. Kincaid and W. Cheney, *Numerical Analysis*, 2nd ed. (Brooks/Cole, 1991).
11. L. D. Landau and E. M. Lifschitz, *Fluid Mechanics* (Pergamon, Elmsford, NY, 1959).
12. J. Lighthill, *Waves in Fluids*, 1st ed. (Cambridge Univ. Press, Cambridge, UK, 1978).
13. M. S. Longuet-Higgins and E. D. Cokelet, The deformation of steep surface waves on water. 1. A numerical method of computation, *Proc. R. Soc. London* **350**, 1 (1976).
14. M. S. Longuet-Higgins and R. W. Stewart, Changes in the form of short gravity waves on long waves and tidal currents, *J. Fluid Mech.* **8**, 565 (1960).
15. D. W. Moore, Resonances introduced by discretization, *IMA J. Appl. Math.* **31**, 1 (1983).

16. T. Nakayama and K. Washizu, Non-linear analysis of liquid motion in a container subjected to forced pitching oscillation, *Int. J. Numer. Methods Eng.* **15**, 1207 (1980).
17. J. N. Newman, *Marine Hydrodynamics* (MIT Press, Cambridge, MA, 1977).
18. J. Peiró, J. Peraire, and K. Morgan, *FELISA System Reference Manual. Part I. Basic Theory*, Civil Eng. Department Report, University of Wales, Swansea, UK, CR/821/94, 1994.
19. J. Peiró, J. Peraire, and K. Morgan, *FELISA System Reference Manual. Part II. Program Manual*, Civil Eng. Deptartment Report, University of Wales, Swansea, UK, CR/822/94, 1994.
20. R. K. Price, The breaking of waves, *J. Geophys. Res.* **76**, 1576 (1971).
21. B. Ramaswamy and M. Kawahara, Arbitrary lagragian-eulerian finite element method for unsteady, convective, incompressible viscous free surface flow, in *Finite Elements in Fluids* (Wiley, New York, 1987), Vol. 7.
22. B. Ramaswamy, M. Kawahara, and T. Nakayama, Lagragian finite element method for the analysis of two-dimensional sloshing problems, *Int. J. Numer. Methods Fluids* **6**, 659 (1986).
23. S. S. Rao, *The Finite Element Method in Engineering* (Pergamon, Elmsford, NY, 1982).
24. A. J. Roberts, A stable and accurate numerical method to calculate the motion of a sharp interface between fuids, *IMA J. Appl. Math.* **31**, 13 (1983).
25. S. J. Sherwin, Hierarchical *hp* finite elements in hybrid domains, *Finite Elements Anal. Design.* **27**, 109 (1997).
26. S. J. Sherwin and G. E. Karniadakis, A triangular spectral element method; applications to the incompressible navier-stokes equations, *Comput. Methods Appl. Mech. Eng.* **123**, 189 (1995).
27. F. Solaas, *Analytical and Numerical Studies of Sloshing in Tanks*, Ph.D. thesis, Trondheim University, 1995.
28. B. Szabo and I. Babuska, *Finite Element Analysis* (Wiley, New York, 1991).
29. D. C. Tolefson and L. Boichet, Free-surface linear water-wave problems by the finite element method, in *2nd Symposium on Naval Hydrodynamics, 1974*.
30. W. Tsai and D. K. P. Yue, Computation of non-linear free-surface flows, *Ann. Rev. Fluid Mech.* **28**, 249 (1996).
31. T. Warburton, *Spectral/hp Methods on Polymorphic Multi-Domains: Algorithms and Applications*, Ph.D. thesis, Brown University, 1999.
32. T. Warburton, S. J. Sherwin, and G. E. Karniadakis, Spectral basis functions for 2D hybrid hp elements, *SIAM J. Numer. Anal.*, in press.
33. G. X. Wu, Hydrodynamic forces on a submerged circular cylinder undergoing large-amplitude motion, *J. Fluid Mech.* **254**, 41 (1993).
34. G. X. Wu and R. Eatock Taylor, Finite element analysis of two-dimensional non-linear transient water waves, *Appl. Ocean Res.* **16**, 363 (1994).
35. G. X. Wu and R. Eatock Taylor, Time stepping solutions of the two-dimensional non-linear wave radiation problem, *Ocean Eng.* **22**(8), 785 (1995).
36. G. X. Wu, Q. W. Ma, and R. Eatock Taylor, Numerical simulation of sloshing waves in a 3d tank based on a finite element method, submitted for publication.
37. R. W. Yeung, Numerical methods in free-surface flows, *Ann. Rev. Fluid Mech.* **14**, 395 (1982).